Nanoscale

Accepted Manuscript

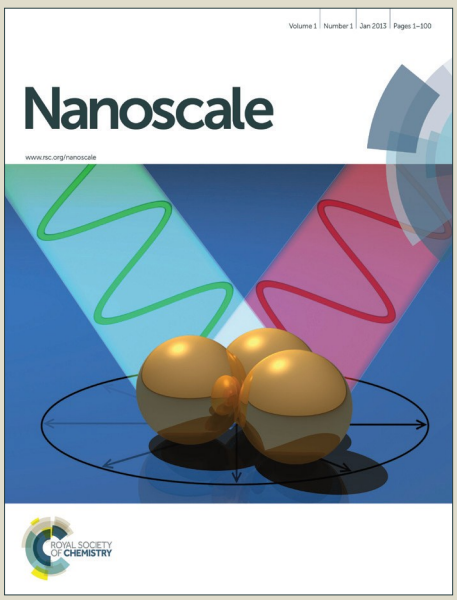

ROYAL SOCIETY OF CHEMISTRY

www.rsc.org/nanoscale

Journal Name

ARTICLE

Levelling the Playing Field: Screening for Synergistic Effects in Coalesced Bimetallic Nanoparticles

Received 00th January 20xx,
Accepted 00th January 20xx

DOI: 10.1039/x0xx00000x

www.rsc.org/

Rachel Lee Siew Tan,[a,b] Xiaohui Song,[a] Bo Chen,[c] Wen Han Chong,[a] Yin Fang,[a] Hua Zhang,[c] Jun Wei,[*,b] and Hongyu Chen[*,a]

Depending on the synthetic methods, bimetallic nanoparticles can have either core-shell, phase segregated, alloy, or partially coalesced structures, presenting different degrees of atomic mixing on their surface. Along with the variations of size and morphology, the structural differences make it difficult to compare the catalytic activity of bimetallic nanoparticles. In this article, we developed a facile screening method that can focus on the synergistic effects rather than structural differences. Prefabricated nanoparticles are mixed together to form linear aggregates and coalesced to form bimetallic junctions. Their hollow silica shells allow materials transport but prevent further aggregation. With a level playing field, this screening platform can identify the best bimetallic combination for a catalytic reaction, before optimizing the synthesis. This approach is more advantageous than the conventional approaches where structural difference may have dominant effects in the catalytic performance.

Introduction

Nanoparticles have been widely used in heterogeneous catalysis for their high surface area,[1, 2] and bimetallic catalysts have recently attracted great attention for the synergistic effects.[3] In comparison to monometallic nanoparticles, bimetallic ones have unique surface binding sites and electronic properties.[4] The juxtaposition of dissimilar atoms on an alloy surface creates a wide range of possibilities of different binding sites, which can be screened for special affinity and synergistic effects in catalysis.[3-5] In addition, the mismatch of atomic sizes in an alloy creates strains and unusual interfaces, sometimes leading to novel electronic property and superior catalytic activity.[1, 6]

With bimetallic systems, the difficulty in catalytic screening increases exponentially with the increase of system complexity. With a wide variety of possible metals, different bimetallic ratios, and complex synthetic parameters, studying a huge number of samples would be impractical without high-throughput screening methods. Most importantly, bimetallic nanoparticles can have either core-shell, phase segregated, alloy, or partially coalesced structures (Figure 1a-d).[7] The huge differences in the number/type of catalytic sites make it difficult to compare and interpret the catalytic performance.

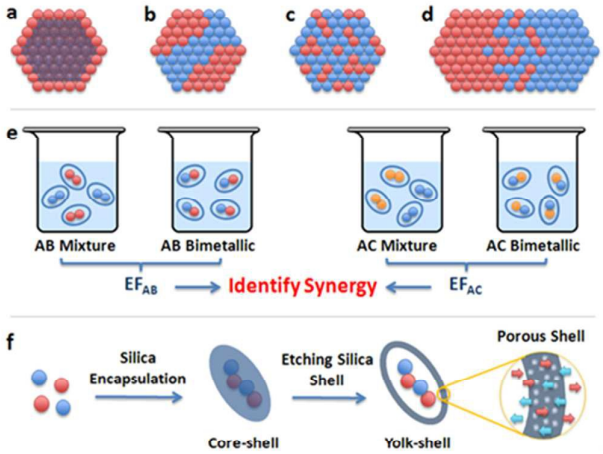

Figure 1. Schematics showing the different types of bimetallic nanoparticles: (a) core-shell; (b) phase-segregated; (c) alloy; and (d) coalesced nanoparticles. Schematics illustrating (e) the comparison of catalytic enhancement, where the bimetallic and the mixture samples have similar structural features; and (f) the silica encapsulation of nanoparticle clusters and the etching to make yolk-shell structures.

In terms of synthesis, two metal salts can be sequentially reduced to create core-shell nanoparticles (the successive reduction method) or simultaneously reduced to enhance mixing (the co-reduction method).[7] The conventional preparation method is to vary the ratio of two metal salts and then apply the co-reduction method. However, the resulting nanostructures vary widely depending on the choice of metals. For example, the more reactive metal is often reduced first, leading to de facto successive reduction and its diminished presence on the nanoparticle surface. In addition, the nucleation and growth[8] of bimetallic nanoparticles vary wildly

[a] Division of Chemistry and Biological Chemistry, Nanyang Technological University, Singapore 637371. Email: hongyuchen@ntu.edu.sg
[b] Singapore Institute of Manufacturing Technology, 71 Nanyang Drive, Singapore 638075. Email: jwei@simtech.a-star.edu.sg
[c] School of Materials Science and Engineering, Nanyang Technological University, Singapore 639798.

Electronic Supplementary Information (ESI) available: (details of any supplementary information available should be included here). See DOI: 10.1039/x0xx00000x

among the combinations,[7] leading to different sizes and thus different total surface area.

Hence, it is difficult to compare bimetallic nanoparticles. The reported catalytic activity (turnover frequency) of a sample essentially groups together the effects of chemical reactivity, surface area, and degree of atomic mixing (Figure 1a-d). The contributions from the structural differences could easily overwhelm the differences in reactivity.[1, 9, 10] More often than not, we are comparing the effects of structures without knowing it.

Considering the large number of bimetallic combinations, it is impractical to achieve consistent size and structure among the samples, and too time consuming to characterize them as such. Well-defined synthesis of even one sample requires searching through *N* dimensional parameter space, including the bimetallic ratio, choice and sequence of the reactants, reaction time, temperature, *etc*.[8, 11, 12] Ideally, we should compare only the intrinsic synergistic effects, so that one could identify the right bimetallic combination before fine-tuning the synthesis. To this end, the challenge is to provide a level ground of comparison, that is, to create comparable controls with the same bimetallic structure, a similar degree of alloying, and similar surface area.

In this work, we design a screening platform with a level playing field. Only one structural type (*i.e.*, the partially coalesced nanoparticle) is fabricated for each bimetallic combination. Using similarly prepared monometallic nanoparticles as the control, all structural factors are made similar so that only the synergistic effect stands out. With the catalytic enhancement directly corresponding to the synergistic effect (Figure 1e), the comparison between bimetallic combinations can be easily carried out.

Results and Discussion

Metal nanoparticles were separately synthesized by reducing the metal salts with $NaBH_4$ in the presence of the weak ligand citrate ions.[13] After purification, two types of metal nanoparticles were mixed and subjected to silica encapsulation, during which they form mixed aggregates in the form of chains (the AB bimetallic sample).[14] The silica-encapsulated nanoparticle clusters were isolated and purified, before they were heated in aqueous solution to make hollow silica shells (Figure 2a),[15, 16] with partial coalescence occurring at the nanoparticle junctions. To prepare a control sample with no bimetallic junctions, each type of nanoparticles was separately aggregated, encapsulated, and etched to form yolk-shell structures; the silica-coated products were then mixed together (the AB mixture sample). The silica shells ensured that there was no further aggregation/coalescence to create bimetallic regions. For easy comparison in validating the screening platform, we used the well-studied catalytic reduction of 4-nitrophenol as the model reaction.

Here, the design principles are as follows: (1) considering the lack of size control and difficulties in the direct synthesis of bimetallic nanoparticles, prefabricated nanoparticles are prepared as stock solutions for easy combination; (2) chain

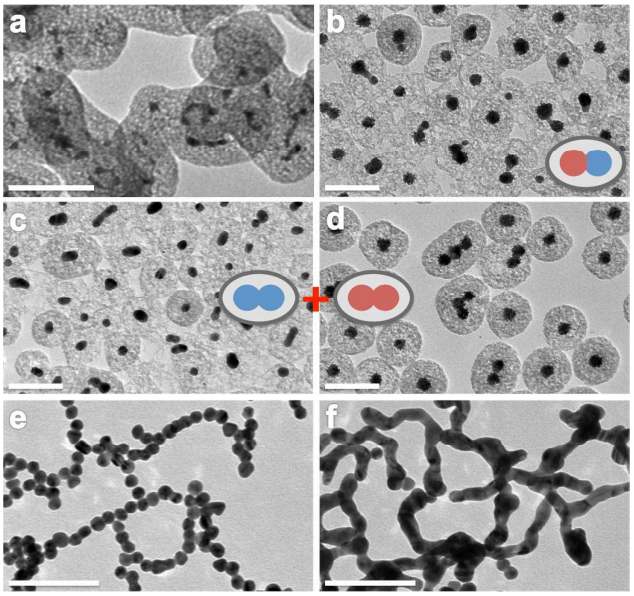

Figure 2. TEM images of (a) 5 nm Au-Pt bimetallic sample; (b) 15-20 nm Au-Pt bimetallic sample; (c) 15 nm Au@silica; (d) 20 nm Pt@silica; and control experiments showing (e) Au nanoparticles mixed with NH_3 (final concentration 140 mM) at room temperature; and (f) Au nanoparticles mixed with NH_3 and heated at 90 ^{o}C for 15 min. All scale bars are 100 nm.

aggregates of nanoparticles (as opposed to globular clusters) expose their junctions; (3) coalescence gives bimetallic region at the junctions; (4) to promote coalescence and ensure clean metal surface for catalysis, the same weak ligand citrate is used; (5) the hollow and porous silica shells allow diffusion of reactants to the metal surfaces and prevent the catalyst from further aggregation during the catalysis; (6) the overall method is still facile with several processes occurring at a same step.

To prepare Au-Pt bimetallic sample for catalysis, 5 nm Au and Pt nanoparticles were mixed, encapsulated, and then the silica shells were etched. The resulting product showed long coalesced network encapsulated in hollow silica shells (Figure 2a). However, due to the small size of the nanoparticles, it was difficult to discern coalescence and to distinguish Au from Pt against the silica shell. As a model study, larger spherical Au nanoparticles (15 nm) and spiky Pt nanoparticles (20 nm) were used. Figure 2b shows the Au-Pt bimetallic sample, whereas 2c and 2d show the separately processed Au and Pt nanoparticles used for the Au-Pt mixture sample. The degree of aggregation was less extensive than the 5 nm nanoparticles, likely due to the stronger charge repulsion between larger particles.[14] Most of these nanoparticles appeared coalesced, judging from the "neck" at the junctions. The coalescence was more significant for the smaller Au nanoparticles (Figure 2c) than the Pt ones (Figure 2d). Owing to the extensive coalescence, the clusters of Au nanoparticles form elongated rods, where the Au-Au junctions can no longer be recognized. In Figure 2b, there were often coalesced small Au domains around the spiky Pt nanoparticles, suggesting successful formation of coalesced bimetallic regions.

Control experiments established that the presence of ammonia and the absence of suitable ligands were responsible

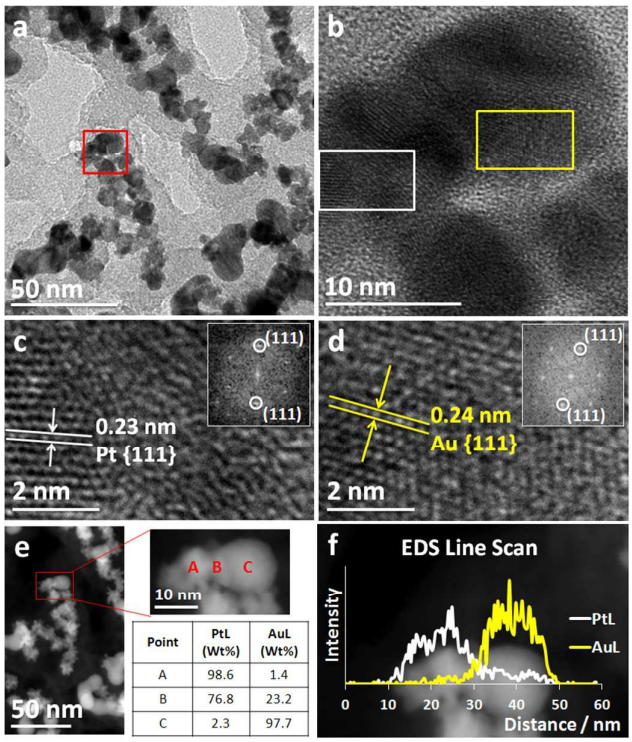

Point	PtL (Wt%)	AuL (Wt%)
A	98.6	1.4
B	76.8	23.2
C	2.3	97.7

Figure 3. TEM analysis of Au-Pt bimetallic sample. Images of (a) Au-Pt bimetallic sample; (b) the Au-Pt junction as marked in red in 3a; (c,d) Pt and Au regions as marked in white and yellow in 3b, respectively, insert are the corresponding FFT patterns; (e) STEM image of the same region as 3a with EDS point scan data tabulated; and (f) EDS line scan of the same region as 3b, showing the mixing of elements at the Au-Pt junction.

for the aggregation of metal nanoparticles during the silica encapsulation. In the literature, single encapsulation of metal nanoparticles in silica typically involved strong vitreophilic ligands,[17-19] which have –SH group on one end and –COOH or –$Si(OR)_3$ group on the other. Such ligands can prevent aggregation and render the metal surface amenable for silica adsorption. In their absence and with only citrate as the ligand, addition of ammonia to a solution of Au nanoparticles immediately (< 5 s) caused it to turn purple, indicating extensive chain aggregation (Figure S1).[14] The immediate colour change indicates that the aggregation of nanoparticles occurs prior to the silica shell formation which takes at least 2 h.[15] The sample was allowed to sit at room temperature for 15 min, the resulting product showed networks made of aggregated spherical nanoparticles, but there was only slight coalescence (Figure 2e). A similarly prepared sample was heated at 90 °C for 15 min, the nanoparticles coalesced extensively such that the junctions can no longer be recognized (Figure 2f). Considering these control experiments, most of the coalescence in our samples should occur at the elevated temperature during the etching step.

It is known that Au nanoparticles grafted with strong ligands at the same aggregated state typically do not coalesce upon heating.[14] We believe that the coalescence here was promoted by direct contact of the particles because the weaker ligand can easily dissociate.[20] The coalescence is thermodynamically

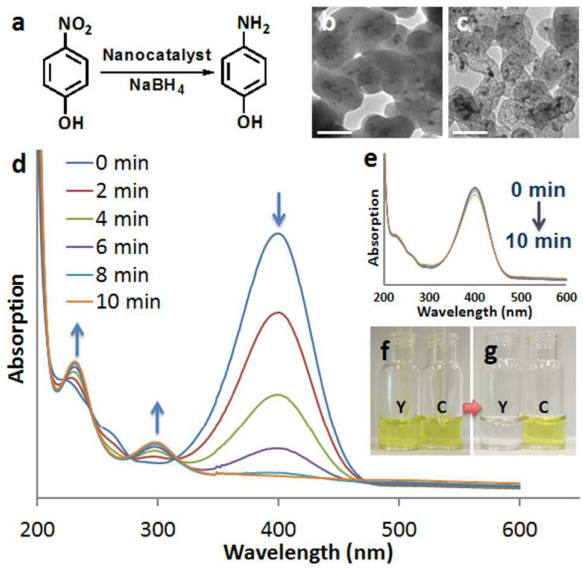

Figure 4. (a) Reaction scheme showing the reduction of 4-nitrophenol to 4-aminophenol. TEM images of (b) core-shell; and (c) yolk-shell structures of the Au-Pd bimetallic sample. Kinetic UV-Vis spectra recorded during the catalysis using (d) yolk-shell; and (e) core-shell Au-Pd bimetallic catalysts. Photos showing the 4-nitrophenol reduction (left: yolk-shell (Y); right: core-shell (C)) at (f) 0 min and (g) 10 min. All scale bars are 100 nm.

driven by the high surface energy at the junction of the nanoparticles,[8] but the kinetics is obviously limited by the inter-particle distance and ligands, among other factors.[21-23]

Figure 3a shows a Au-Pt bimetallic sample (15 nm Au nanoparticles and 20 nm Pt nanoparticles) with extensive aggregation. The spiky and spherical nanoparticles were randomly distributed within the clusters and the sphere-sphere junctions were completely coalesced. Away from the coalesced junctions, the Pt {111}[24] and Au {111}[25] lattice fringes obtained by high-resolution TEM (HRTEM) and fast Fourier transform (FFT) analysis were consistent with those of Au and Pt lattices (Figure 3c,d). Figure 3b shows a Pt-Au interparticle junction, which was completely filled up as a result of coalescence. Scanning transmission electron microscopy (STEM) and electron dispersive X-ray spectroscopy (EDS) were performed for the same region to study the elemental distribution. The EDS line scan (Figure 3f) implies the gradual mixing of the elements near the junction, which was further supported by EDS point scans with elemental ratios (Figure 3e and S3).

The hollow silica shell was intended to prevent aggregation of the clusters but allow efficient materials transport (Figure 1f). While solid silica shells are known to be microporous, they are not porous enough for a fast catalytic reaction. We compared a non-etched (core-shell, Figure 4b) to an etched sample (hollow yolk-shell, Figure 4c) in catalyzing the reduction of 4-nitrophenol (Figure 4a). With the yolk-shell sample, the absorption peak at 400 nm decreases with time and two new peaks at 226 nm and 305 nm appeared, indicating the formation of 4-aminophenol (Figure 4d).[26] In contrast, for the core-shell sample, there was no colour change (Figure 4f,g)

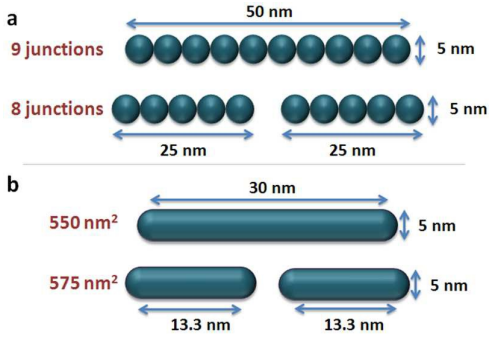

Figure 5. Schematics comparing (a) the number of junctions and (b) the total surface area of long and short nanoparticle clusters. The total volume of metal is kept the same.

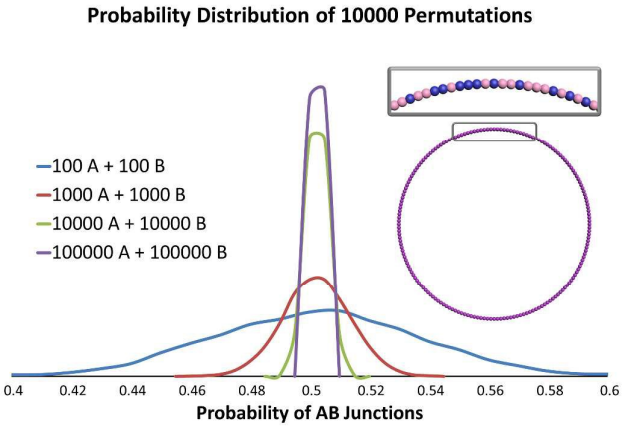

Figure 6. Probability distributions of AB junctions when A and B particles are randomly lined up into a circle. 10000 permutations were carried out for samples containing 200, 2000, 20000, and 200000 nanoparticles, respectively.

and the decrease of absorption peak at 400 nm was minimal (Figure 4e), suggesting hindered accessibility.

For catalytic screening, we separately synthesized Au, Ag, Pt, and Pd nanoparticles using the $NaBH_4$ reduction method. The different reaction rates led to different nanoparticle sizes: the Pt and Pd nanoparticles were below 5 nm in diameter; the Au nanoparticles were around 5 nm; and the Ag nanoparticles were about 10-20 nm (Figure S4). From these stock solutions, the bimetallic sample and the mixture sample were prepared and their severe aggregation was verified by TEM (Figure S5). After etching and coalescence, the chains appeared only slightly thicker than the original nanoparticle diameters. The coalescence is expected to be more extensive than the model study with larger nanoparticles, considering the larger surface energy of the smaller particles and the shorter distances (smaller junctions) required for the coalescence.

Considering that all samples contain chain aggregates, their total surface area should be similar and insensitive to the extent of aggregation. Comparing a 10-particle chain to two 5-particle chains (Figure 5a), the longer aggregate has only one more junction than the shorter ones and about 4% less surface area after the coalescence (Figure 5b).

For a simple estimate, we assume random arrangements and ignore the small difference caused by the two ends of a chain. When starting from 0.5*N* A and 0.5*N* B nanoparticles (*N* is a large number), the bimetallic sample is expected to have roughly 0.5*N* AB bimetallic junctions and 0.25*N* AA and 0.25*N* BB homo-metallic junctions, whereas the mixture sample should have roughly 0.5*N* AA and 0.5*N* BB homo-metallic junctions. Hence, comparing the bimetallic and the mixture samples, the major difference is the number of bimetallic junctions. They have the same mole of metal atoms and started from the same batch of nanoparticles (hence the same size and morphology). Moreover, the number of junction and surface area should be all similar.

The number of nanoparticles in our experiments is estimated to be around 3.73 trillion for each metal. Given the large number, the probability of giving AB, AA, and BB junctions should not vary significantly among different batch of samples. In an idealized *in silico* model, all nanoparticles in a sample were randomly lined up to form a circle (Figure 6) and we ran 10000 permutations to study the probability distribution in forming the AB junctions. When the sample contained only 200 nanoparticles, the ratio of AB junctions varied noticeably among the batches. When the sample size increased to 2000, 20,000 and 200,000 nanoparticles, the variance narrows significantly to around 0.1% standard deviation. For our samples with greatly more nanoparticles, the deviation arising from the random distribution is expected to be much less than the normal errors of other experimental conditions. Control experiments with 5 batches of Ag-Pd bimetallic sample confirmed that the deviation in catalytic performance was indeed small (Figure S11).

The fact that we have different sizes of nanoparticles will affect the total surface area of each type of metal, for example, the Ag:Au area ratio will not be 1:1 even though the same mole of atoms were present in a sample. But it will not cause a difference in the number of junction and surface area if we compare the bimetallic sample to the mixture sample.

An enhancement factor (EF) can be defined as the ratio of the turnover frequencies (TOF) of the bimetallic sample to that of the mixture sample. On the bases of the above analyses, the only difference between the two samples is the presence and absence of bimetallic junctions. Hence, the catalytic enhancement corresponds directly to the additional synergistic effects. An EF >1 would suggest positive synergistic effects and EF < 1 suggests negative effects. When comparing the different bimetallic combinations, a larger EF suggests better synergistic effects. It should be noted that in a bimetallic nanoparticle, the alloy surface constitute around 25% of its total surface. Hence, the EF of the model system is about only 1/4 of a perfect bimetallic alloy. In the literature, researchers interested in unique facets often compared TOF per surface atoms, whereas those interested in overall catalytic performance compared TOF per atom. In our case, because both the factors are the same in the bimetallic and the mixture samples, the comparison is much simpler and on a level ground. Indeed, as shown in Eq. 2, the EF is simply inversely proportional to the reaction time.

$$\text{TOF} = \frac{\text{moles of product}}{\text{moles of catalyst} \times \text{reaction time } (t)} \quad (1)$$

$$\text{EF} = \frac{\text{TOF of bimetallic}}{\text{TOF of mixture}} = \frac{t \text{ of mixture}}{t \text{ of bimetallic}} \quad (2)$$

Starting from the stock solutions of Au, Ag, Pt and Pd nanoparticles, there are total 6 combinations; each with two samples, i.e., the bimetallic and the mixture samples. Figure S6-S9 gives the kinetic UV-Vis spectra showing the reduction of 4-nitrophenol using the bimetallic and the mixture sample as the catalyst. The resulting TOFs per total atom and the EFs were tabulated (Table 1).

Table 1. Catalytic performance of the metal nanoparticles, the bimetallic and the mixture samples.

Metals	Moles of Metal Atoms	Reaction Time (s)	TOF (s^{-1})
Au	2.92×10^{-8}	600	1.22×10^{-3}
Ag	2.92×10^{-8}	300	2.44×10^{-3}
Pt	2.92×10^{-8}	-	-
Pd	2.92×10^{-8}	180	5.94×10^{-3}

Metal Combination	Moles of Metal Atoms	TOF of Mixture (s^{-1})	TOF of Bimetallic (s^{-1})	Enhancement Factor (EF)
Au-Ag	2.92×10^{-8}	3.05×10^{-3}	4.07×10^{-3}	1.33
Au-Pd	2.92×10^{-8}	1.53×10^{-3}	1.53×10^{-3}	1
Au-Pt	2.92×10^{-8}	-	-	-
Ag-Pd	1.46×10^{-9}	24.4×10^{-3}	30.5×10^{-3}	1.25
Ag-Pt	1.46×10^{-9}	17.4×10^{-3}	20.4×10^{-3}	1.17
Pd-Pt	2.92×10^{-8}	2.44×10^{-3}	2.04×10^{-3}	0.83

Amount of 4-nitrophenol is fixed at 2.14×10^{-8} mol (2.14 mM).

As shown in Table 1, the presence of Ag can enhance the catalytic activity of Au, Pt, and Pd, which is consistent with the literature observations.[27-29] The reaction of Ag-Pt and Ag-Pd was too fast for us to accurately measure the reaction time, so we used 1/20 of the catalyst concentration while maintaining all other conditions unchanged. On the other hand, Pt catalyses fast degradation of $NaBH_4$, leading to H_2 evolution rather than the intended reduction of 4-nitrophenol.[30] As a result, the reaction using Au-Pt catalysts did not go to completion. The same happened when only monometallic Pt sample (similarly aggregated and coated in silica) was used (Figure S6d).

Hence, these results validate our screening platform. With this method, we intend to create a large combination and prepare the samples in parallel. The synthesis of individual nanoparticles can be easily scaled up. Starting from the stock solutions, the mixing of the nanoparticles, the silica encapsulation, and the etching step, can be easily carried out in parallel in small volume (typically < 1 mL in eppendorf tubes). Hence, it would not be difficult to screen hundreds of samples, except that UV-Vis monitoring of the reaction is the rate-limiting step.

A simple solution is to use visual observation for the initial screening. As shown in Figure 7a, the colour change of the 4-nitrophenol was obvious enough to make initial judgments, reducing the number of possibilities for further screening. To facilitate the process, video recording system was set up (Figure 7b) so that one does not have to start all the reactions at the same time. The time span could be easily marked during the playback. With candidates emerging from the first level of screening, detailed UV-Vis characterizations can verify the results and provide more precise measurements.

A further improvement is to adapt automated sample addition system using multi-well microplates and microplate reader,[31, 32] so that dozens of samples can run in parallel. As a proof-of-concept, we performed a small scale screening using a multiplate reader and an 8-channel multipipette (Figure 7d). The temporal evolution of the 400 nm absorption was monitored for four combinations of bimetallic and mixture samples (Figure 7c). The results were well consistent with the above detailed studies. It is conceivable that other catalytic reactions with characteristic fluorescence or UV-Vis-NIR peaks can be similarly studied.

Conclusions

In summary, this work focused on the methodology development, towards a level-field comparison of the catalytic performance of bimetallic nanoparticles. We have demonstrated that 1) the nanoparticles can form linear aggregates and coalesce; 2) the hollow silica shells protect the clusters while allowing materials transport; 3) the bimetallic and the mixture samples have the same structure type, similar size and surface area; and 4) high-throughput catalytic screening is feasible and the findings are consistent with the literature reports. We believe that it will be cost-effective to identify the right combination with synergistic effects, before optimizing the synergy. To this end, an evaluating platform with a level playing field is of critical importance.

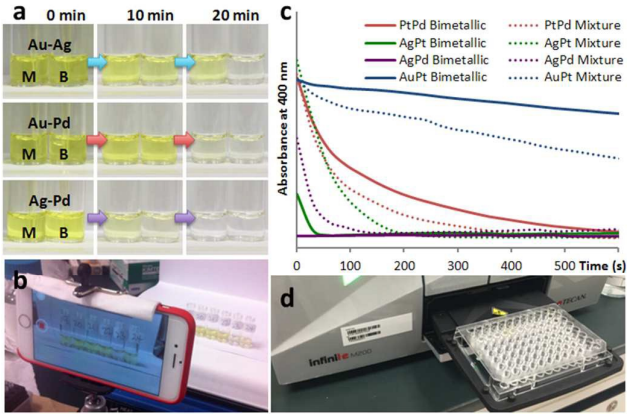

Figure 7. (a) Photos of the mixture sample (M) and the bimetallic sample (B) after adding 4-nitrophenol and $NaBH_4$, for Au-Ag; Au-Pd, and Ag-Pd combinations. Photos of (b) the set up for video recording; and (c) UV-Vis absorption trace at 400 nm for 4 combinations recorded using a multi-plate reader (d) Photo of the 96-microwell plate used in multi-plate reader.

Experimental

Materials

Sodium tetrachloropalladate(II), silver nitrate, chloroplatinic acid hexahydrate, hydrogen tetra-chloroaurate trihydrate, trisodium citrate dihydrate, citric acid, L-ascorbic acid, sodium borohydride, tetraethyl orthosilicate (TEOS), isopropanol (IPA), and ammonia (30 wt.%) were purchased from Sigma Aldrich and used without purification. DI water (resistivity of 18.2 MΩ•cm) was used in all experiments.

Methods

Preparation of Au nanoparticles. 15 nm Au nanoparticles were synthesized according to a modified method reported by G. Frens.[33] 100 mL of DI water was preheated at 110 ^{o}C for 10 min in a 250 mL round bottom flask with vigorous stirring. 1 mL of $HAuCl_4.3H_2O$ (10 mg/mL) was added into the flask and heated for another 10 min. 3 mL of 1 wt.% sodium citrate was added into the reaction flask. Reaction was vigorously stirred and heated at 110 ^{o}C for another 30 min and cooled down to room temperature before use.

Preparation of Pt nanoparticles. 20 nm Pt nanoparticles were synthesized according to Bigall et al.[34] 3.6 mL of $H_2PtCl_6.6H_2O$ (0.2 wt.%) was added to 46.6 mL of boiling DI water in a round bottom flask with vigorous stirring and heating at 110 ^{o}C. 1.1 mL of a solution consisting of 1 wt.% sodium citrate and 0.05 wt.% citric acid was added into the reaction mixture followed by the addition of $NaBH_4$ solution (0.08 wt.%) containing 1 wt.% sodium citrate and 0.05 wt.% citric acid. Reaction mixture was heated for another 10 min under vigorous stirring before cooling down to room temperature. This solution was used as seed to prepare 20 nm Pt nanoparticles.

1 mL of the above seed solution was added into 29 mL of DI water at room temperature. 20 µL of $H_2PtCl_6.6H_2O$ (400 mM) was added into the reaction flask followed by the addition of 0.5 mL of solution containing L-ascorbic acid (1.25 wt.%) and sodium citrate (1 wt.%). The reaction flask was heated up to boiling point with vigorous stirring and allowed to react for a total of 30 min and cooled down to room temperature.

Preparation of metallic nanoparticles for catalysis. 250 µL of metal salt (50 mM) was added to 50 mL of DI water under vigorous stirring, followed by the addition of 400 µL of sodium citrate (1 wt.%). 1550 µL of $NaBH_4$ (100 mM) was added to the reaction mixture. Solution was kept under vigorous stirring for another 10 min.

Preparation of AB bimetallic samples by silica encapsulation of metallic nanoparticles via Stöber method. 1 mL of metal nanoparticles A and 1 mL of metal nanoparticles B were centrifuged and redispersed into 600 µL of DI water. The solution was added into a reaction vial containing 1 mL of IPA and 2 µL TEOS and the mixture was vortexed. 40 µL of ammonia (30 wt.%) was added to promote silica encapsulation.

Preparation of monometallic samples by silica encapsulation of metallic nanoparticles via Stöber method. 2 mL of metal nanoparticles A was centrifuged and redispersed into 600 µL of DI water. The solution was added into a reaction vial containing 1 mL of IPA and 2 µL TEOS and the mixture was vortexed. 40 µL of ammonia (30 wt.%) was added to promote silica encapsulation.

Formation of yolk-shell nanoparticles. 1 mL of the silica-encapsulated nanoparticles was purified with centrifugation twice at 10000 rpm for 15 min and redispersed in 500 µL of DI water. Solution was heated at 90 °C for 15 min. The product was isolated by centrifugation and redispersed into 100 µL of DI water.

Preparation of AB mixture samples. After formation of yolk-shell structures, 15 µL of monometallic sample A was mixed with 15 µL of monometallic sample B.

Catalytic reduction of 4-nitrophenol using visual screening method. 10 µL catalyst and 300 µL of DI water were placed in a 2 mL reaction vial. 100 µL of 4-nitrophenol (15 mM) and 600 µL of $NaBH_4$ (300 mM) was vortex and mixed. 200 µL of this mixture was added into the vial with catalyst. Color change was observed with video recording.

Catalytic reduction of 4-nitrophenol using UV-Vis spectrometer. 100 µL of 4-nitrophenol (15 mM) and 600 µL of $NaBH_4$ (300 mM) was vortex and mixed. 10 µL of this mixture was diluted with 590 µL of DI water in a microcuvette. 10 µL of metal nanoparticles catalyst was carefully mixed into the microcuvette. Kinetic UV-Vis spectra were collected at 1 min interval. 20 scans were performed for each sample.

Catalytic reduction of 4-nitrophenol using multiplate reader. 100 µL of 4-nitrophenol (15 mM) and 600 µL of $NaBH_4$ (300 mM) was vortex and mixed. 10 µL of this mixture was diluted with 190 µL of DI water. Eight portions of this mixture were prepared. Disposable 96 microwells plate was used for this characterization. 5 µL of catalyst was added into each well. Using an 8-channel pipette, the above mixture was added into each well. Kinetic UV-Vis absorption at 400 nm wavelength was collected at 30 s interval. 50 scans were performed for each sample (temporal evolution of the 400 nm absorption is reported in Figure S10).

Characterizations

Transmission electron microscopy (TEM) images were obtained with a JEM-1400 (JEOL). JEM-2100F (JEOL) coupled with electron dispersive x-ray spectrometer (EDS) was used to obtain high resolution TEM (HRTEM) images and EDS elemental mapping. Ultraviolet-Visible (UV-Vis) spectra were obtained with a Cary 100 spectrophotometer. Temporal evolution of the 400 nm absorption was monitored with Infinite M200 (Tecan) multiplate reader.

Acknowledgements

The research was supported by A*STAR (SERC 112-120-2011) and MOE (RG14/13) of Singapore. The authors thank Dr. Haiyan Xu for the probability computation used in Figure 6.

Notes and references

1. W. Yu, M. D. Porosoff and J. G. Chen, *Chem. Rev.*, 2012, **112**, 5780-5817.
2. W. Huang, J. H.-C. Liu, P. Alayoglu, Y. Li, C. A. Witham, C.-K. Tsung, F. D. Toste and G. A. Somorjai, *J. Am. Chem. Soc.*, 2010, **132**, 16771-16773.
3. L.-C. Lee, C. Xiao, W. Huang and Y. Zhao, *New J. Chem.*, 2015, **39**, 2459-2466.
4. M. Sankar, N. Dimitratos, P. J. Miedziak, P. P. Wells, C. J. Kiely and G. J. Hutchings, *Chem. Soc. Rev.*, 2012, **41**, 8099-8139.
5. C. Chen, Y. Kang, Z. Huo, Z. Zhu, W. Huang, H. L. Xin, J. D. Snyder, D. Li, J. A. Herron, M. Mavrikakis, M. Chi, K. L. More, Y. Li, N. M. Markovic, G. A. Somorjai, P. Yang and V. R. Stamenkovic, *Science*, 2014, **343**, 1339-1343.
6. A. K. Singh and Q. Xu, *ChemCatChem*, 2013, **5**, 652-676.
7. R. Ferrando, J. Jellinek and R. L. Johnston, *Chem. Rev.*, 2008, **108**, 845-910.
8. Y. Wang, J. He, C. Liu, W. H. Chong and H. Chen, *Angewandte Chemie International Edition*, 2015, **54**, 2022-2051.
9. N. A. Dehm, X. Zhang and J. M. Buriak, *Inorg. Chem.*, 2010, **49**, 2706-2714.
10. N. A. Beckers, S. Huynh, X. Zhang, E. J. Luber and J. M. Buriak, *ACS Catal.*, 2012, **2**, 1524-1534.
11. X. Liu, D. Wang and Y. Li, *Nano Today*, 2012, **7**, 448-466.
12. X. Liu and X. Liu, *Angew. Chem. Int. Ed.*, 2012, **51**, 3311-3313.
13. N. R. Jana, L. Gearheart and C. J. Murphy, *J. Phys. Chem. B*, 2001, **105**, 4065-4067.
14. M. Yang, G. Chen, Y. Zhao, G. Silber, Y. Wang, S. Xing, Y. Han and H. Chen, *PCCP*, 2010, **12**, 11850-11860.
15. Y. J. Wong, L. Zhu, W. S. Teo, Y. W. Tan, Y. Yang, C. Wang and H. Chen, *J. Am. Chem. Soc.*, 2011, **133**, 11422-11425.
16. X. Song, T. Ding, L. Yao, M. Lin, R. L. Siew Tan, C. Liu, K. Sokol, L. Yu, X. W. Lou and H. Chen, *Small*, 2015, **11**, 4351-4365.
17. H. Wang, L. Chen, Y. Feng and H. Chen, *Acc. Chem. Res*, 2013, **46**, 1636-1646.
18. C. Xue, X. Chen, S. J. Hurst and C. A. Mirkin, *Adv. Mater.*, 2007, **19**, 4071-4074.
19. S. P. Mulvaney, M. D. Musick, C. D. Keating and M. J. Natan, *Langmuir*, 2003, **19**, 4784-4790.
20. J. Xu, Y. Wang, X. Qi, C. Liu, J. He, H. Zhang and H. Chen, *Angew. Chem. Int. Ed.*, 2013, **52**, 6019-6023.
21. H. Zhang and D. Wang, *Angewandte Chemie*, 2008, **120**, 4048-4051.
22. M. Jose-Yacaman, C. Gutierrez-Wing, M. Miki, D.-Q. Yang, K. Piyakis and E. Sacher, *The Journal of Physical Chemistry B*, 2005, **109**, 9703-9711.
23. P. Grammatikopoulos, C. Cassidy, V. Singh and M. Sowwan, *Scientific Reports*, 2014, **4**, 5779.
24. X. Xiang, W. He, L. Xie and F. Li, *Catal Sci Technol*, 2013, **3**, 2819-2827.
25. G. Plascencia-Villa, D. Bahena, A. R. Rodriguez, A. Ponce and M. Jose-Yacaman, *Metallomics*, 2013, **5**, 242-250.
26. J. He, W. Ji, L. Yao, Y. Wang, B. Khezri, R. D. Webster and H. Chen, *Adv. Mater.*, 2014, **26**, 4151-4155.
27. T. Wu, L. Zhang, J. Gao, Y. Liu, C. Gao and J. Yan, *J. Mater. Chem. A*, 2013, **1**, 7384-7390.
28. H. You, Z. Peng, J. Wu and H. Yang, *Chem. Commun.*, 2011, **47**, 12595-12597.
29. L. Zhou, Z. Liu, H. Zhang, S. Cheng, L.-J. Fan and W. Ma, *Nanoscale*, 2014, **6**, 12971-12980.
30. J. Zhang, G. Chen, D. Guay, M. Chaker and D. Ma, *Nanoscale*, 2014, **6**, 2125-2130.
31. L. M. Magalhaes, C. Nunes, M. Lucio, M. A. Segundo, S. Reis and J. L. F. C. Lima, *Nat. Protocols*, 2010, **5**, 1823-1830.
32. B. K. McKenna, A. A. Selim, F. Richard Bringhurst and D. J. Ehrlich, *Lab Chip*, 2009, **9**, 305-310.
33. G. Frens, *Nature*, 1973, **241**, 3.
34. N. C. Bigall, T. Härtling, M. Klose, P. Simon, L. M. Eng and A. Eychmüller, *Nano Letters*, 2008, **8**, 4588-4592.